2R.4 **THE EVOLUTION OF FINE-SCALE BOUNDARIES ON 15 JUNE 2002 DURING IHOP**

Brian Monahan* and Yvette P. Richardson
The Pennsylvania State University, University Park, PA

Joshua M. Wurman
Center for Severe Weather Research, Boulder, CO

1. INTRODUCTION

One of the fundamental motivations for the convection initiation (CI) component of the International H2O Project (IHOP), conducted during the spring of 2002 in the Great Plains region of the United States, was to obtain both spatially and temporally high resolution observations of the wind and moisture fields in the convective boundary layer (CBL). To meet these objectives, IHOP employed a vast network of both ground-based and airborne instrumentation within and surrounding an intensive observation region (IOR), including multiple mobile Doppler radars, atmospheric profilers, and lidars. In addition, the regional synoptic scale surface observation network, rawindsonde stations, satellite, and National Weather Service Doppler Radar (WSR-88D) were also utilized in the successful execution of the project.

A data set featuring the interaction between several fine-scale atmospheric boundaries (indicated by lines of convergence) embedded within a strong south-southwesterly flow was obtained by the mobile armada between approximately 1850 UTC and 2220 UTC on 15 June 2002. Convection did initiate near the IOR late in the afternoon on 15 June; however, the focus of this study is the evolution of the convective boundary layer (CBL) and mesoscale boundaries in the hours prior to CI. In particular, multiple convective modes exist in the boundary layer during the day's first deployment, with evidence of both prominent horizontal convective rolls (HCR) and cellular convection in the multi-Doppler wind syntheses at different times. This leads to one of the fundamental questions of 15 June: what role do the CBL structures play in augmenting convergence and, by extension, vertical motion through interaction with the mesoscale boundaries present? Additionally, an interesting comparison between the organization of convective motions before and after the merger of several mesoscale boundaries is presented.

2. SYNOPTIC OVERVIEW

The operations plan for 15 June 2002 called for a focus of resources across the central Oklahoma panhandle as an area of low pressure was forecast to develop along the leeward side of the Rocky Mountains in response to a mid level shortwave trough moving southeastward from the Great Basin. Indeed, at 1200 UTC, a rather weak low pressure center, with mean sea level pressure near 1008 hPa, was observed across northeastern New Mexico and southeastern Colorado. Extending eastward into south-central Kansas was a diffuse warm front, highlighted by a fairly subtle wind shift as well as a minimal moisture gradient. Additionally, along and just to the north of the front, convection was ongoing in parts of central Kansas. To the south of the front, dewpoints were near 15°C across southern Kansas and northern Oklahoma while slightly drier air was poised just to its north, with dewpoints ranging between 10-13°C.

Much farther south, across the IOR, temperatures rose only slowly throughout the morning hours as a result of cloud debris left over from the previous day's convection. By late morning, as mixing began to occur through the lower levels of the troposphere, skies became mainly clearly allowing temperatures to warm to 27-29°C by 1800 UTC. Surface winds increased markedly as this mixing process ensued; throughout the afternoon hours of 15 June 2002, winds were between 10-15 m s^{-1} with gusts to near 18 m s^{-1}. The strong surface winds appear to play a critical role in the organization of the horizontal convective rolls observed early in the first deployment. Also noted in the visible satellite imagery are periodic fields of small cumulus during the early afternoon hours; in general, though, these cloud fields dissipated relatively quickly. By the time of the mobile radar deployment, temperatures had warmed substantially, ranging from 30-33°C across the central Oklahoma panhandle. Additionally, at the start of the first deployment, approximately 1900 UTC, surface dewpoints actually rose slightly across the IOR to between 15-18°C. However, as mixing of the lower troposphere continued through the mid to late afternoon hours, drier air was noted at the surface, with dewpoints once again hovering near 15°C by the end of the day.

3. RADAR ANALYSIS METHODS

Data from several ground-based mobile Doppler radars are used in creating analyses of the three-dimensional wind field on 15 June 2002. Data are included from two Doppler on Wheels (DOW) radars and the XPOL radar, all having 3 cm wavelength, 0.93° beam width, and 90 second volume updates (Wurman et al., 1997). Data were collected in one-half degree increments in elevation between 0.5° and 4.5°, one degree increments between 5.5° and 11.5°, and 1.5° increments between 13.0° and 14.5°. In future work, data from the Shared Mobile Atmospheric Research and Teaching Radar (SMART-Radar) and the National

*_Corresponding Author Address_: Brian Monahan, Department of Meteorology, Penn State University, University Park, PA 16802; e-mail: bpm157@psu.edu

Center for Atmospheric Research's S-Band Dual Polarization Doppler Radar (SPOL) will be introduced.

Following the removal of ground clutter, range-folded echoes, and numerous side lobes, which most notably were present in the higher beam elevations above ground level, the radial velocity field of each radar was de-aliased. As the radar data are collected in the field on a truck-relative coordinate system, it is necessary to rotate the data such that they are relative to true north prior to objectively analyzing the data. To accomplish this, the solar alignment technique suggested by Arnott et al. (2003) was applied. Finally, following the suggestions of Matejka (2002), a reference velocity was used to adjust data locations to those valid at a chosen reference time, generally the center time of the volume.

Data were then objectively analyzed to a 40 x 40 x 1.5 km^3 grid using an isotropic spherical Barnes weighting function within the REORDER program. Consistent with the suggestions of Koch et al. (1983) and Trapp and Doswell (2000), grid spacing of 100 meters and a smoothing parameter of 0.184 km^2 was chosen based on the desired response for wavelengths two times the coarsest resolution in the analysis domain. A radius of influence of 0.699 km was used based on the suggestions of Pauley and Wu (1990). Finally, over-determined dual-Doppler wind syntheses were produced by using the National Center for Atmospheric Research's (NCAR) CEDRIC to perform an iterative upward integration of the mass continuity equation subject to a lower boundary condition of zero vertical velocity. Extrapolation of data was prevented by requiring valid information from at least five octants surrounding a particular grid point.

4. OBSERVATIONS

One of the most interesting features on 15 June 2002 is the presence of a combination of convective modes in the first deployment. Evident in reflectivity data and the synthesized convergence field, both horizontal convective rolls, which are oriented approximately parallel to the mean wind through the depth of the analysis domain (southwest-to-northeast), and cellular convection are observed (Fig. 1). Consistent with the counter-rotating nature of HCRs, the horizontal vorticity vector at 300 m AGL is oriented approximately parallel to the rolls in alternating directions. Curiously, the relatively weak vertical wind shear vector at the same level is oriented nearly perpendicular to the HCRs; this might best be explained as a manifestation not of the low-level environmental wind shear, but rather shear due to the roll circulations themselves. Interestingly, as the first deployment evolves, the dominant convective mode appears to alternate between HCRs and cellular convection. For example, by 1936 UTC it is fairly difficult to discern the presence of horizontal convective rolls, but a pattern of cellular convection is identifiable in both the convergence and vertical motion fields (Fig. 2). By 1940 UTC, however, a far less prominent HCR structure seems to reemerge.

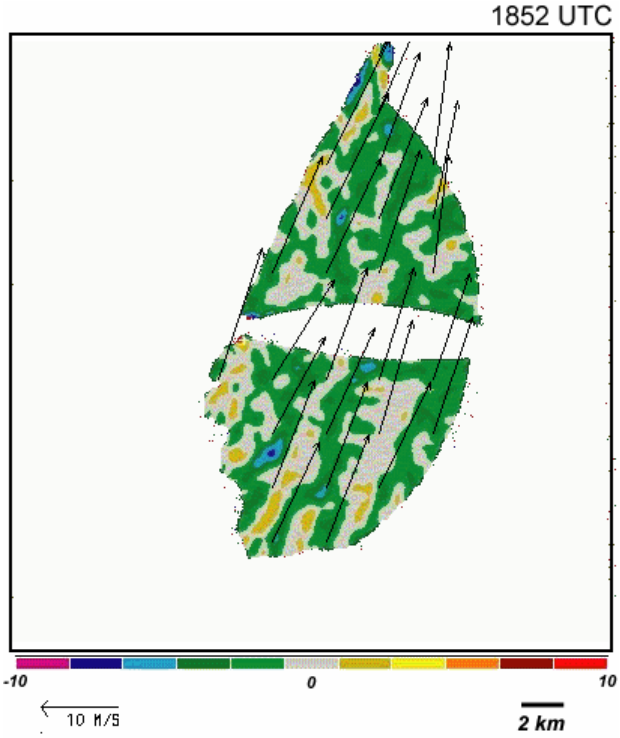

Figure 1: Divergence and horizontal wind vectors plotted at 300 m AGL at 1852 UTC. Note the HCR structures are parallel to the wind.

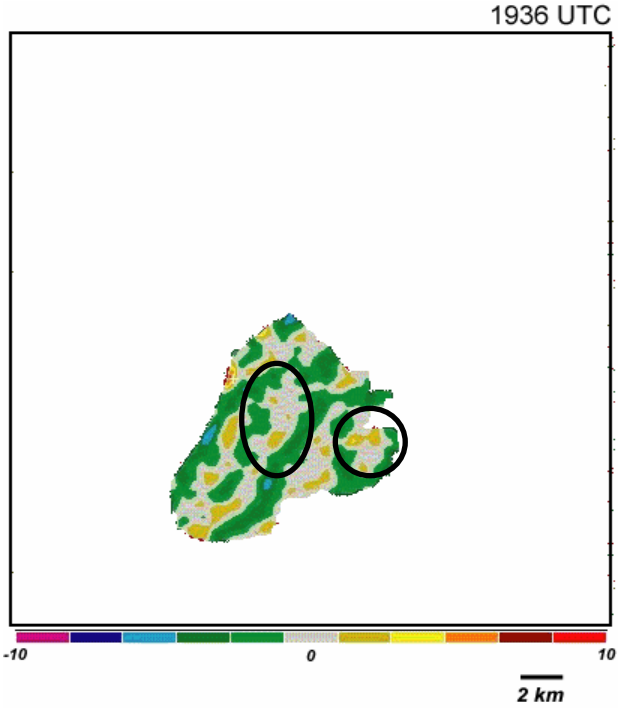

Figure 2: Divergence plotted at 300 m AGL at 1936 UTC. While there is still some sense that horizontal convective rolls are present, there also now appears to be evidence of convergence patterns resembling cellular convection, as indicated by the circles.

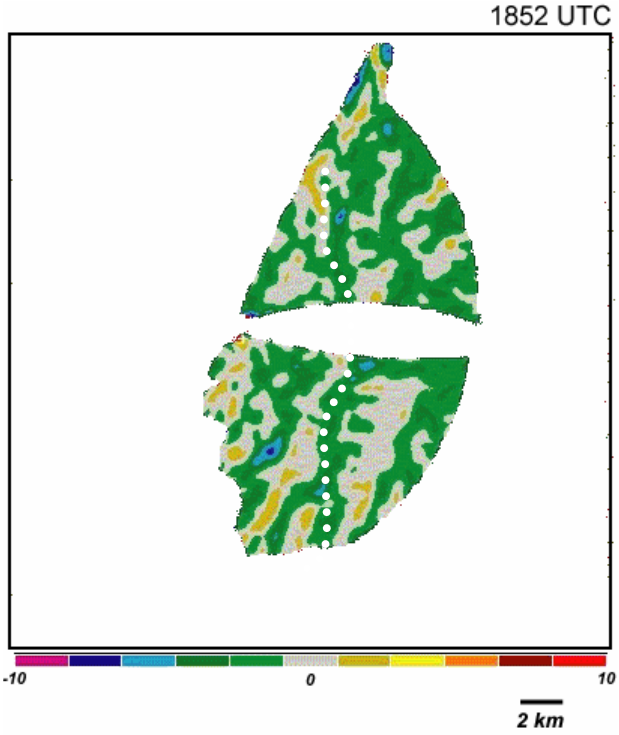

Figure 3: Divergence plotted at 300 m AGL at 1852 UTC. Maxima in convergence appear draped from northeast to southwest across the analysis domain. A fractured linear maximum in convergence, boundary B, is also observed as highlighted by the dashed white line.

Embedded within the field of horizontal convective rolls and cellular convection are multiple fine-scale boundaries, evident as both reflectivity and convergence maxima. At 1852 UTC, the start of the day's first deployment, a prominent south-to-north boundary (boundary A) is observed through the east-central part of the analysis domain. Additionally, to the west of boundary A is a fractured linear maximum in convergence that appears to correspond to a second, weaker boundary (boundary B) aligned parallel to the far more prominent boundary A (Fig. 3).

Throughout the first deployment, spanning 1852 UTC to 1942 UTC, convergence along the horizontal convective rolls and, indeed, through the remainder of the analysis domain is generally observed to be less than 2 x 10^{-3} s^{-1} at 300 m AGL. As boundary B propagates toward the northeast, it appears that convergence is enhanced where the boundary intersects the horizontal convective rolls. For example, at 1900 UTC, convergence maxima of up to 6 x 10^{-3} s^{-1} are noted where these intersections occur (Fig. 4a). Furthermore, vertical vorticity is also enhanced in the immediate vicinity of intersections between boundary B and horizontal convective rolls, as vertical vorticity values are observed to locally exceed 6 x 10^{-3} s^{-1} (Fig. 4b).

By 1904 UTC, it becomes apparent that a third boundary (boundary C) is present across the far western part of the analysis domain (not shown). Due to the geometry of the deployment, it is unclear whether boundary C forms in the analysis domain or merely propagates into it. Convergence along the length of this boundary is nearly 2 x 10^{-3} s^{-1} with maxima that slightly exceed 4 x 10^{-3} s^{-1}.

Where convergence, and thus vertical motion, is locally enhanced, cloud development might be anticipated given sufficient moisture. Likely resulting from moderate convective inhibition (CIN), as indicated by a mid level (between 650-700 hPa) inversion observed by the mobile radiosonde units, only a few small cumuli are noted in the center of the analysis domain at 1854 UTC. However, prominent cumulus fields are observed to the east and west of the analysis domain. Where clouds do appear in the domain, though, they are generally co-located with convergence maxima of 2-4 x 10^{-3} s^{-1}, most notably in the southwest corner of the domain (not shown). Later, at 1915 UTC, cumulus development has become more pronounced across the eastern half of the analysis domain. By this time, boundary B has moved east of the analysis domain, nearly merging with boundary A. Now, though, much of the cumulus development is focused along boundary C (Fig. 5).

In the first deployment, only a very subtle wind shift is noted across each of the boundaries west of boundary A; however, after the radars re-deploy to the east, a new, merged boundary is noted to have a fairly noticeable wind shift associated with it (Fig. 6), likely owing to the presence of another pre-existing boundary. At 2030 UTC, convergence values along the new, merged boundary (boundary D), are generally between 2-4 x 10^{-3} s^{-1} at 300 m AGL. As this boundary propagates across the domain, winds shift from the south-southwest ahead of the boundary to the southwest behind the boundary, as evidenced by the enhancement in the u-wind component across the western half of the domain. Along boundary D, updrafts at 600 m AGL are observed to generally be less than 1 m s^{-1}, although maxima to between 1-2 m s^{-1} are also noted.

One of the more striking features of boundary D is the presence of multiple kinks, as observed in both the reflectivity data and in the convergence field. Not surprisingly, numerous vertical vorticity maxima are found to be embedded within these kinks along the boundary. At 300 m AGL, for example, vertical vorticity maxima of up to 6 x 10^{-3} s^{-1} are observed, with multiple weaker misocyclones also present along the boundary.

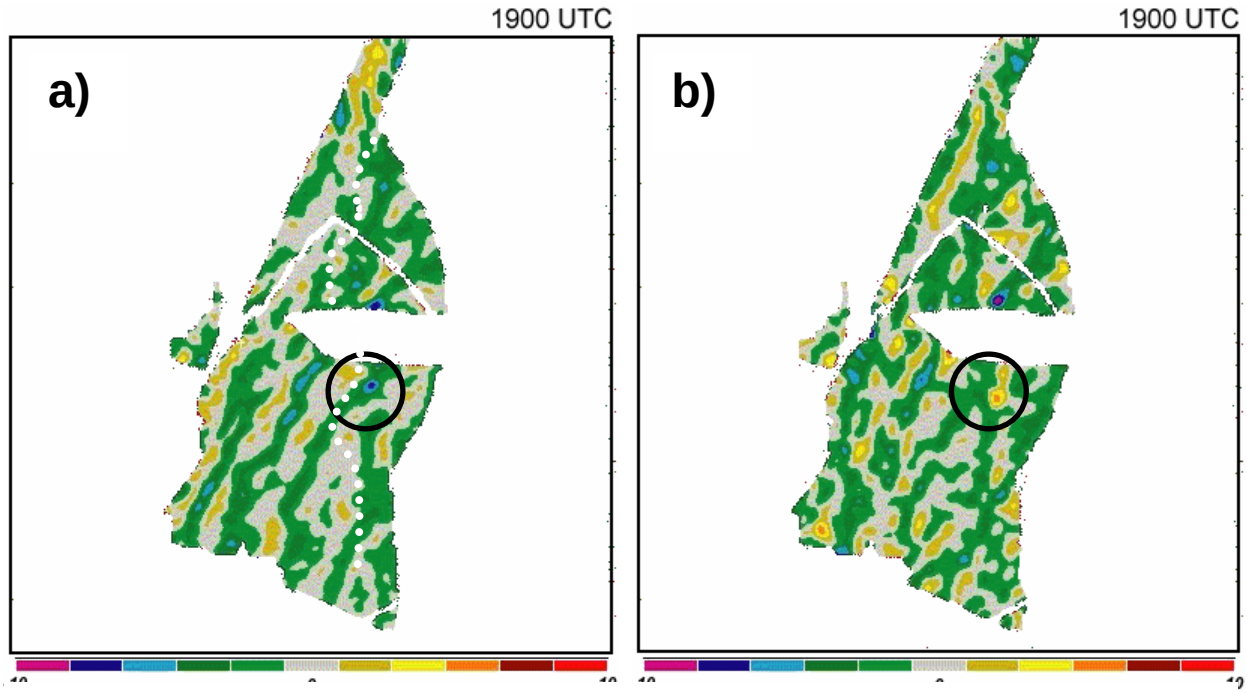

Figure 4: a) Divergence plotted at 300 m AGL at 1900 UTC and b) Vertical vorticity plotted at 300 m AGL at 1900 UTC. Note that where boundary B intersects a horizontal convective roll, as illustrated by the circle, both convergence and vertical vorticity are enhanced. Boundary B is plotted as the white dashed line in a).

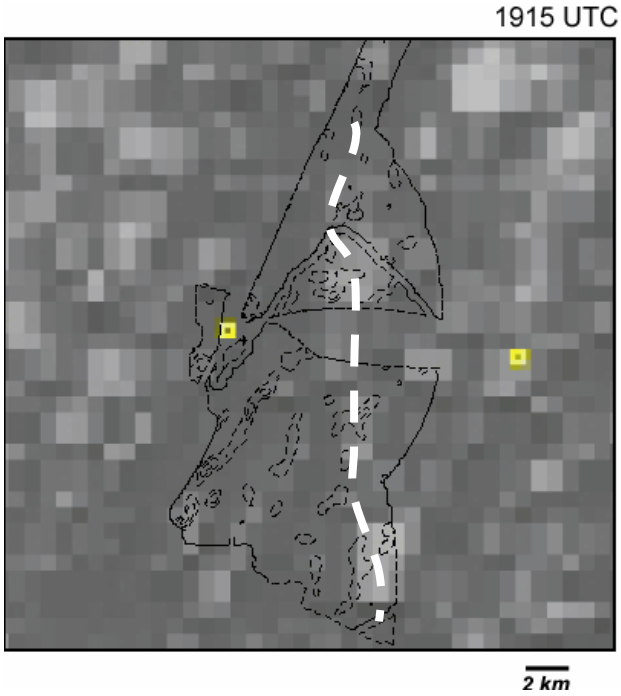

Figure 5: Visible satellite imagery (1 km) at 1915 UTC with divergence at 300 m AGL contoured. The contour interval is 2 s^{-1}, with values less than or equal to -2 s^{-1} plotted. Boundary C is indicated by the dashed line; note the relatively significant cumulus development along this boundary. The location of DOW2 (left-most yellow box) and DOW3 (right-most yellow box) are indicated.

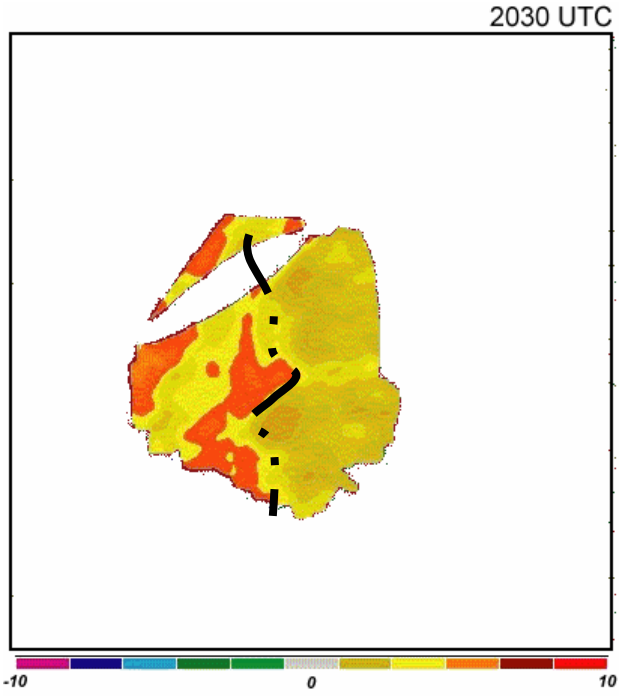

Figure 6: U-wind component plotted at 300 m AGL at 2030 UTC. By this time, several of the fine-scale boundaries had merged to the east of the initial deployment. Across this new boundary, boundary D, a notable wind shift from south-southwest to southwest is observed. The location of boundary D is indicated by the dashed black line.

5. SUMMARY AND FUTURE WORK

In this preliminary study of boundary layer convection across the central Oklahoma panhandle on 15 June 2002, multiple notable features are observed. In the first deployment, three separate boundaries are observed to be embedded within a boundary layer featuring a mixture of horizontal convective rolls and cellular convection. These boundaries, most notably the two weaker ones, and the HCRs appear to interact on a number of occasions, resulting in an enhancement in convergence, upward vertical motion, and vertical vorticity at select locations throughout the analysis domain. Future work will include establishing the relationship, if any, between horizontal convective rolls and the formation and sustenance of the two weaker boundaries (boundaries B and C).

A merger between three separate boundaries is observed across the eastern half of the analysis domain during the first deployment. In the second, post-merger deployment, the horizontal convective roll structure observed earlier is no longer present, leading to a more cellular organization of motions in the convective boundary layer. Future work will quantify this change in CBL structure and attempt to determine the factors controlling convective mode.

In an effort to better understand the low level kinematic and thermodynamic fields associated with each boundary, future work will also include overlaying mobile mesonet data with the completed wind syntheses to establish surface thermodynamic characteristics. Additionally, the relationship between the cloud field and convergence will be further explored. Finally, to better understand the organization of the low-level moisture field, specific humidity data derived from refractivity, as described by Fabry et al. (1997), will be retrieved utilizing the National Center for Atmospheric Research's S-Band Dual Polarization Doppler Radar (SPOL) and will be overlayed with the wind fields.

ACKNOWLEDGEMENTS

Thanks to Paul Markowski and Nettie Arnott for providing several computer codes as well as a number of helpful suggestions. Discussions with Jeff Frame and Jim Marquis were also helpful in bringing a number of features of this data set to light. Also, we are grateful for the tireless work of the IHOP crew members, without whom this study would not have been possible. This work was supported by National Science Foundation Grant ATM-0208651.

REFERENCES

Arnott, N., Y. Richardson, J. Wurman, and J. Lutz, 2003: A solar calibration technique for determining radar pointing angles. Preprints, *31st Conference on Radar Meteorology*, Seattle, Amer. Meteor. Soc., 492-494.

Fabry, F., C. Frush, I. Zawadzki, and A. Kilambi, 1997: On the extraction of near-surface index of refraction using radar phase measurements from ground targets. *J. Atmos. Oceanic Technol.*, **13**, 978-987.

Koch, S. E., M. desJardins and P. J. Kocin, 1983: An interactive Barnes objective map analysis scheme for use with satellite and conventional data. *J. Appl. Meteor.*: **22**, 1487-1503.

Matejka, T., 2002: Estimating the most steady frame of reference from Doppler radar data. *J. Atmos. Oceanic Technol.*, **19**, 1035-1048.

Pauley, P. M., and X. Wu, 1990: The theoretical, discrete and actual response of the Barnes objective analysis scheme for one- and two-dimensional fields. *Mon. Wea. Rev.*: **118**, 1145-1164.

Trapp, J. R., and C. Doswell, 2000: Radar data objective analysis. *J. Atmos. Oceanic Technol*., **17**, 105-120.

Wurman, J., J. Straka, E. Rasmussen, M. Randall, and A. Zahrai, 1997: Design and deployment of a portable, pencil-beam, pulsed, 3-cm Doppler radar. *J. Atmos. Sci.*, **14**, 1502-1512.